

Model-Based Electrochemical Estimation and Constraint Management for Pulse Operation of Lithium Ion Batteries

Kandler A. Smith, Christopher D. Rahn, and Chao-Yang Wang

Abstract—High-power lithium ion batteries are often rated with multiple current and voltage limits depending on the duration of the pulse event. These variable control limits, however, are difficult to realize in practice. In this paper, a linear Kalman filter based on a reduced order electrochemical model is designed to estimate internal battery potentials, concentration gradients, and state-of-charge (SOC) from external current and voltage measurements. A reference current governor predicts the operating margin with respect to electrode side reactions and surface depletion/saturation conditions responsible for damage and sudden loss of power. The estimates are compared with results from an experimentally validated, 1-D, nonlinear finite volume model of a 6 Ah hybrid electric vehicle battery. The linear filter provides, to within $\sim 2\%$, performance in the 30%–70% SOC range except in the case of severe current pulses that draw electrode surface concentrations to near saturation and depletion, although the estimates recover as concentration gradients relax. With 4 to 7 states, the filter has low-order comparable to empirical equivalent circuit models commonly employed and described in the literature. Accurate estimation of the battery's internal electrochemical state enables an expanded range of pulse operation.

Index Terms—Electrochemical model, lithium ion battery, model reduction, reference governor, state-of-charge (SOC) estimation.

I. INTRODUCTION

MODEL-BASED battery monitoring algorithms enable efficient and reliable integration of batteries into hybrid electric vehicle (HEV) powertrains. Examples include the generalized recursive least squares algorithm of Verbrugge *et al.* [1] and the extended Kalman filter algorithm of Plett [2]. Both algorithms use an assumed empirical battery model to predict state-of-charge (SOC) and maximum pulse power available within some fixed, predetermined voltage limits. In pulsed-power applications, fixed current/voltage limits can be overly conservative, particularly for short-duration, high-rate current pulses that give rise to large ohmic voltage perturbations [3].

Manuscript received November 18, 2006. Manuscript received in final form June 30, 2009. First published September 22, 2009; current version published April 23, 2010. Recommended by Associate Editor A. G. Stefanopoulou. This work was supported by the U.S. Department of Energy, Office of FreedomCAR and Vehicle Technologies, Graduate Automotive Technology Education Program. This work was performed at the Pennsylvania State University.

K. A. Smith is with the National Renewable Energy Laboratory, Golden, CO 80401 USA (e-mail: kandler@hotmail.com; kandler_smith@nrel.gov).

C. D. Rahn and C.-Y. Wang are with the Department of Mechanical and Nuclear Engineering, The Pennsylvania State University, University Park, PA 16802 USA (e-mail: cdrahn@psu.edu; cxw31@psu.edu).

Digital Object Identifier 10.1109/TCST.2009.2027023

Manufacturers sometimes rate high-power batteries with multiple current/voltage limits that depend on the duration of the pulse event [4]. These control limits are difficult to realize in practice.

For lithium ion (Li-ion) batteries, the 1-D model of Doyle *et al.* [5], [6], derived from porous electrode and concentrated solution theories, captures relevant solid-state and electrolyte diffusion dynamics and accurately predicts current/voltage response. The model also predicts physical limits of charge and discharge, namely, saturation/depletion of Li concentration at the electrode surfaces, $c_{s,e}$, and depletion of Li concentration in the electrolyte solution, c_e . To avoid sudden loss of power, a control algorithm must maintain Li concentrations within constraints

$$0 < \frac{c_{s,e}(x,t)}{c_{s,\max}} < 1, \quad c_e(x,t) > 0.$$

To avoid damaging side reactions, the solid/electrolyte phase potential difference, $\phi_{s-e} = \phi_s - \phi_e$, must be maintained within constraints

$$U_{side\ rxn, deinsertion} < \phi_{s-e}(x,t) < U_{side\ rxn, insertion}$$

where $U_{side\ rxn}$ is the equilibrium potential of a side reaction occurring when Li ions are either inserted into or deinserted from active material particles.

The reference governor [7] is an effective method to control a system within constraints and has been used, for example, to prevent fuel cell oxygen starvation by dynamically limiting fuel cell load current [8]. In the case of a battery, in which *in situ* measurement of internal concentration and potential is not possible, proximity to internal constraints must be estimated using current and voltage measurements. Derivation of a dynamic electrochemical model suitable for battery state estimation is difficult, however, given the infinite dimensionality of the underlying partial differential equation (PDE) system. By spatially discretizing the PDEs, distributed parameter-type estimation algorithms have been developed for the lead-acid battery [9] and the nickel-metal hydride battery [10], though with high order (30–100 states) in comparison to the more commonly used equivalent circuit model-based algorithms (2–5 states).

Recently, the authors used a model order reduction technique to develop a low- (~ 7 th) order Li-ion battery model in state variable form [11], [12] directly from the physical governing equations of Doyle *et al.* [5], [6]. This work employs that model in

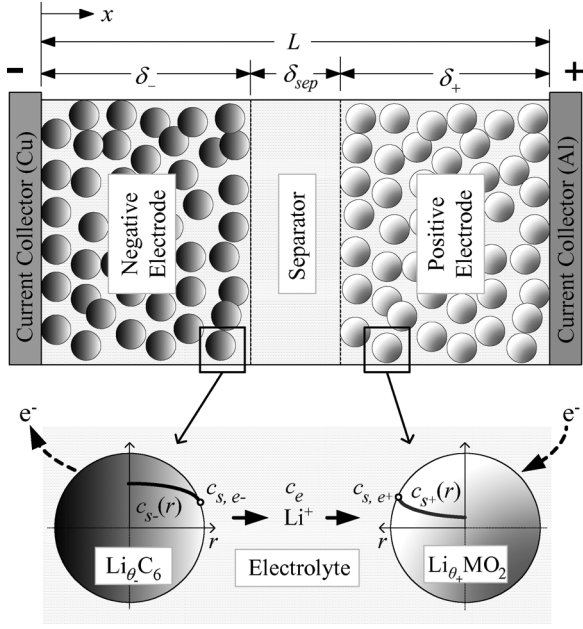


Fig. 1. Schematic of Li-ion battery during discharge.

a linear state estimation and reference governor algorithm relevant for pulse power applications in which batteries are operated in a moderate SOC range. SOC estimates and pulse current/power limits are demonstrated, using a high-order nonlinear finite-volume model (FVM) of a 6 Ah HEV cell to simulate the plant.

II. MODEL AND FILTER EQUATIONS

Fig. 1 shows a schematic of the 1D battery model [5], [6], [11]. During discharge, Li ions diffuse to the surface of carbon particles in the negative electrode where they react and transfer to an electrolyte solution. The positively charged ions travel via diffusion and migration through the electrolyte solution, where they again react and diffuse into metal oxide active material particles. Electrons, produced in the negative electrode reaction and consumed in the positive electrode reaction, are blocked by the electronically insulating separator and instead must travel through an external circuit.

A. Infinite-Dimensional Time Domain Model

The electrochemical model parameters are defined in Table I. The 1-D electrochemical model consists of four PDEs describing the conservation of Li in the solid phase (written for a spherical active material particle with reaction current j^{Li} from the surface)

$$\frac{\partial c_s}{\partial t} = \frac{D_s}{r^2} \frac{\partial}{\partial r} \left(r^2 \frac{\partial c_s}{\partial r} \right) \quad (1)$$

$$D_s \frac{\partial c_s}{\partial r} \Big|_{r=R_s} = \frac{-j^{Li}}{a_s F} \quad (2)$$

conservation of Li in the electrolyte phase

$$\frac{\partial(\epsilon_e c_e)}{\partial t} = \frac{\partial}{\partial x} \left(D_e \frac{\partial c_e}{\partial x} \right) + \frac{1-t_+^o}{F} j^{Li} \quad (3)$$

 TABLE I
MODEL PARAMETERS FOR 6 AH LI-ION HEV BATTERY

Parameter	Symbol	Negative Electrode	Separator	Positive Electrode
Thickness [cm]	δ	50×10^{-4}	25.4×10^{-4}	36.4×10^{-4}
Particle radius [cm]	R_s	1×10^{-4}		1×10^{-4}
Solid phase Li diffusion coefficient [cm ² /s]	D_s	2.0×10^{-12}		3.7×10^{-12}
Active material volume fraction	ϵ_s	0.580		0.500
Solid phase conductivity [S/cm]	σ^{eff}	$1.0 \epsilon_s$		$0.1 \epsilon_s$
Charge transfer resistance [Ω cm ²]	R_{ct}	7.14		9.88
Maximum solid phase concentration [mol/cm ³]	$c_{s,max}$	16.1×10^{-3}		23.9×10^{-3}
Stoichiometry at 0% SOC	$\theta_{0\%}$	0.126		0.936
Stoichiometry at 100% SOC	$\theta_{100\%}$	0.676		0.442
Electrolyte volume fraction	ϵ_e	0.332	0.5	0.330
Bruggeman tortuosity exponent	p	1.5	1.5	1.5
Parameter	Symbol	Value		
Electrolyte phase Li ⁺ diffusion coefficient [cm ² /s]	D_e^{eff}	$D_e = 2.6 \times 10^{-6}$, $D_e^{eff} = D_e \epsilon_e^p$		
Electrolyte phase ionic conductivity [S/cm]	κ^{eff}	$\kappa = 15.8 c_e \exp(0.85(1000 c_e)^{1.4})$, $\kappa^{eff} = \kappa \epsilon_e^p$		
Average electrolyte concentration [mol/cm ³]	$c_{e,0}$	1.2×10^{-3}		
Li ⁺ transference number	t_+^o	0.363		
Electrode plate area [cm ²]	A	10452		
Foil contact resistance [Ω cm ²]	R_f	20		
Negative Electrode Equilibrium Potential [V]	U_-	$U_-(\theta) = 8.00229 + 5.0647\theta - 12.578\theta^{1/2}$ $- 8.6322 \times 10^{-4} \theta^{-1} + 2.1765 \times 10^{-2} \theta^{3/2}$ $- 0.46016 \exp[15.0(0.06 - \theta)]$ $- 0.55364 \exp[-2.4326(\theta - 0.92)]$		
Positive Electrode Equilibrium Potential [V]	U_+	$U_+(\theta) = 85.681\theta^6 - 357.70\theta^5 + 613.89\theta^4$ $- 555.65\theta^3 + 281.06\theta^2 - 76.648\theta$ $- 0.30987 \exp(5.657\theta^{115.0}) + 13.1983$		

$$\frac{\partial c_e}{\partial x} \Big|_{x=0} = \frac{\partial c_e}{\partial x} \Big|_{x=L} = 0 \quad (4)$$

conservation of charge (e^-) in the solid phase (active material particle/binder matrix)

$$\frac{\partial}{\partial x} \left(\sigma \frac{\partial \phi_s}{\partial x} \right) - j^{Li} = 0 \quad (5)$$

$$-\sigma \frac{\partial \phi_s}{\partial x} \Big|_{x=0} = \sigma \frac{\partial \phi_s}{\partial x} \Big|_{x=L} = \frac{I(t)}{A} \quad (6)$$

and conservation of charge in the electrolyte phase

$$\frac{\partial}{\partial x} \left(\kappa \frac{\partial \phi_e}{\partial x} \right) + \frac{\partial}{\partial x} \left(\kappa_D \frac{\partial \ln c_e}{\partial x} \right) + j^{Li} = 0 \quad (7)$$

$$\frac{\partial \phi_e}{\partial x} \Big|_{x=0} = \frac{\partial \phi_e}{\partial x} \Big|_{x=L} = 0. \quad (8)$$

The four PDEs are coupled by the Butler–Volmer equation describing the reaction current at the solid/electrolyte interface

$$j^{Li} = a_s i_o \left\{ \exp \left[\frac{\alpha_a F}{RT} \eta \right] - \exp \left[-\frac{\alpha_c F}{RT} \eta \right] \right\} \quad (9)$$

as a function of overpotential

$$\eta = \phi_s - \phi_e - U. \quad (10)$$

In (10), note that the phase potential difference must overcome the equilibrium potential of the electrode surface $U = U(c_{s,e})$ in order to drive the reaction current in (9). Voltage measured across the battery terminals

$$V(t) = \phi_s(L, t) - \phi_s(0, t) - \frac{R_f}{A} I(t) \quad (11)$$

includes an empirical contact resistance between the electrode and current collector.

Under sustained discharge, $I < 0$, concentration and potential gradients reduce the electromotive force $V(t)$ of the battery. At complete equilibrium (which may take hours to achieve following even a brief discharge or charge event), all gradients relax ($\eta = \Delta\phi_e = \Delta c_s = \Delta c_e = 0$), and (11) reduces to the so-called open-circuit voltage

$$V_{OC} = U_+(c_{s,avg+}) - U_-(c_{s,avg-}). \quad (12)$$

The battery's available stored charge or SOC is determined by the average concentration of Li in each electrode. Equation (12) can be expressed solely as a function of battery SOC using conservation relationships. Lumping each electrode and applying (solid-phase) Li and charge conservation provides a linear relationship between the negative and positive electrode-averaged concentrations

$$I(t) = -\delta_- \varepsilon_s - AF \frac{dc_{s,avg-}}{dt} = \delta_+ \varepsilon_s + AF \frac{dc_{s,avg+}}{dt} \quad (13)$$

valid at all times. For estimation purposes, the electrode-averaged concentrations are normalized and written as a linear function of SOC

$$c_{s,avg}(t) = [\text{SOC}(t)(\theta_{100\%} - \theta_{0\%}) + \theta_{0\%}] c_{s,max} \quad (14)$$

where $\theta = c_s/c_{s,max}$ is the dimensionless solid-state Li concentration (henceforth, stoichiometry) of each electrode, and $\theta_{0\%}$ and $\theta_{100\%}$ are reference values at 0% and 100% SOC, respectively. Note that, by substituting the time derivative of (14) into (13), one recovers the ampere-hour integration-type definition of SOC more commonly found in the estimation literature

$$I(t) = -Q \frac{d(\text{SOC})}{dt} \quad (15)$$

where $Q = \delta \varepsilon_s AF c_{s,max} |\theta_{100\%} - \theta_{0\%}|$ is the used capacity window of each electrode, also equivalent to overall battery capacity.

B. Infinite-Dimensional Impedance Model

As a preliminary step to model order reduction, transfer function/matrix solutions are derived with current as input and electrochemical field variables as outputs. Solutions for individual field variables are then combined to predict battery voltage.

The solid-state diffusion impedance of a single spherical electrode active material particle is [13]

$$\frac{\bar{c}_{s,e}(s)}{\bar{j}^{Li}(s)} = \frac{1}{a_s F} \left(\frac{R_s}{D_s} \right) \left[\frac{\tanh(\beta)}{\tanh(\beta) - \beta} \right] \quad (16)$$

where $\beta = R_s \sqrt{s/D_s}$, and the overbars indicate Laplace transformed variables. Dimensionless impedance $v(s)$ of an electrode is [14]

$$v(s) = \delta \left(\frac{1}{\kappa} + \frac{1}{\sigma} \right)^{\frac{1}{2}} \left(\frac{R_{ct}}{a_s} + \frac{\partial U}{\partial c_s} \left(\frac{\bar{c}_{s,e}(s)}{\bar{j}^{Li}(s)} \right) \right)^{-\frac{1}{2}} \quad (17)$$

In the present work, equilibrium potential $U(c_{s,e})$ and charge transfer resistance $R_{ct} \approx \eta/j^{Li}$ are each linearized at the 50% SOC rest condition.

Define dimensionless electrode position as $z = x/\delta$, where $z = 0$ is the current collector interface and $z = 1$ is the separator interface. For current $I(t)$ applied at the battery terminals, the authors derived 1-D transcendental functions [12] for reaction rate j^{Li}

$$\frac{\bar{j}^{Li}(z, s)}{\bar{I}(s)} = \frac{1}{\delta A} \frac{1}{\kappa + \sigma} \frac{v(s)}{\sinh v(s)} \times \{ \kappa \cosh [v(s)(z - 1)] + \sigma \cosh [v(s)z] \} \quad (18)$$

overpotential

$$\frac{\bar{\eta}(z, s)}{\bar{I}(s)} = \frac{R_{ct}}{a_s} \frac{\bar{j}^{Li}(z, s)}{\bar{I}(s)} \quad (19)$$

electrode surface minus bulk concentration difference $\Delta c_{s,e} = c_{s,e} - c_{s,avg}$

$$\frac{\Delta \bar{c}_{s,e}(z, s)}{\bar{I}(s)} = \frac{\bar{c}_{s,e}(s)}{\bar{j}^{Li}(s)} \frac{\bar{j}^{Li}(z, s)}{\bar{I}(s)} - \frac{\bar{c}_{s,avg}(s)}{\bar{I}(s)} \quad (20)$$

and electrode bulk concentration $c_{s,avg}$

$$\frac{\bar{c}_{s,avg}(s)}{\bar{I}(s)} = -\frac{1}{\delta A \varepsilon_s F} \frac{1}{s} \quad (21)$$

Equations (18)–(21) are written for the negative electrode and are derived under the assumption of uniform electrolyte concentration. For the positive electrode, one can multiply the right-hand sides of (18)–(21) by -1 .

Analytical solutions for electrolyte concentration and potential are unduly cumbersome. Spatial discretization of (3) and (4) followed by Laplace transformation yields the transfer matrix

$$\frac{\bar{\mathbf{c}}_e(s)}{\bar{\mathbf{I}}(s)} = (\mathbf{K}_{c_e} + s\mathbf{M}_{c_e})^{-1} \mathbf{M}_{c_e} \frac{\bar{\mathbf{J}}^{Li}(s)}{\bar{\mathbf{I}}(s)}. \quad (22)$$

In (22), \mathbf{K}_i , \mathbf{M}_i , and \mathbf{F}_i are the stiffness, mass, and forcing matrices defined by the finite element method, and $\bar{\mathbf{c}}_e(s)$ and $\bar{\mathbf{J}}^{Li}(s)$ are $n \times 1$ vectors representing field variables $\bar{c}_e(x, s)$ and $\bar{j}^{Li}(x, s)$ at discrete node points x_i . Similar treatment of (7) and (8) yields the transfer matrix

$$\frac{\Delta \bar{\boldsymbol{\varphi}}_e(s)}{\bar{\mathbf{I}}(s)} = (\mathbf{K}_{\phi_e})^{-1} \left(-\mathbf{K}_{\phi_e}^{\kappa D} \frac{\bar{\mathbf{c}}_e(s)}{\bar{\mathbf{I}}(s)} + \mathbf{F}_{\phi_e} \frac{\bar{\mathbf{J}}^{Li}(s)}{\bar{\mathbf{I}}(s)} \right). \quad (23)$$

The complete current/voltage impedance model is

$$\begin{aligned} \frac{\bar{V}(s)}{\bar{I}(s)} = & \frac{1}{\text{AF}} \left(\frac{\partial U_+}{\partial c_{s+}} \frac{1}{\delta_+ \varepsilon_{s+}} - \frac{\partial U_-}{\partial c_{s-}} \frac{1}{\delta_- \varepsilon_{s-}} \right) \frac{1}{s} \\ & - \frac{\frac{\partial U_-}{\partial c_{s-}} \Delta \bar{c}_{s,e}(0, s) + \bar{\eta}(0, s) - \Delta \bar{\phi}_{e-}^{jL_i}(0, s)}{\bar{I}(s)} \\ & + \frac{\frac{\partial U_+}{\partial c_{s+}} \Delta \bar{c}_{s,e}(L, s) + \bar{\eta}(L, s) + \Delta \bar{\phi}_{e+}^{jL_i}(L, s)}{\bar{I}(s)} \\ & + \frac{\Delta \bar{\phi}_e^{c_e}(L, s)}{\bar{I}(s)} - \frac{R_f}{A} \end{aligned} \quad (24)$$

with respective terms related to SOC dynamics, negative electrode solid diffusion dynamics, positive electrode solid diffusion dynamics, electrolyte diffusion dynamics, and contact resistance static impedance.

Though the solution is not presented here, it is possible to obtain an analytical infinite series solution for (24). The solution can be made rational by discarding terms having either small magnitude or high frequency [11]. The present vehicular application requires bandwidth of 0 to ~ 10 Hz. Within this limited frequency range, however, a truncated version of the impedance model (24) still has tens of thousands of terms with distinct eigenvalues and nonnegligible residues. For practical application, its order must be further reduced.

C. Reduced-Order State Variable Realization

Following the procedure in [11], a full-order transfer matrix $\bar{y}(s)/\bar{u}(s)$ is reduced to

$$\frac{\bar{y}^*(s)}{\bar{u}(s)} = \mathbf{z} + \sum_{k=1}^n \frac{\mathbf{r}_k s}{s - p_k} \quad (25)$$

with steady-state vector \mathbf{z} obtained from the full-order model as $\mathbf{z} = \lim_{s \rightarrow 0} \bar{y}(s)/\bar{u}(s)$, and poles p_k and residue vectors \mathbf{r}_k numerically generated by minimizing the cost function

$$\begin{aligned} J = & \sum_{k=1}^m \sum_{i=1}^n |\text{Re}(\bar{y}_i^*(j\omega_k) - \bar{y}_i(j\omega_k))|^2 \\ & + |\text{Im}(\bar{y}_i^*(j\omega_k) - \bar{y}_i(j\omega_k))|^2 \end{aligned} \quad (26)$$

across frequency range $\omega \in [0, 2\pi f_c]$, where f_c is the model cutoff frequency chosen by the designer. The reduced-order single-input, multiple-output (SIMO) state variable model

$$\begin{aligned} \dot{\hat{\mathbf{x}}} &= \mathbf{A}\hat{\mathbf{x}} + \mathbf{B}u \\ \mathbf{y}^* &= \mathbf{C}\hat{\mathbf{x}} + \mathbf{D}u + \mathbf{y}_0 \end{aligned} \quad (27)$$

with input u , output \mathbf{y} , and state variable vector \mathbf{x} , is constructed with

$$\begin{aligned} \mathbf{A} &= \text{diag}[\lambda_1 \cdots \lambda_n] \\ \mathbf{B} &= [1 \cdots 1]^T \\ \mathbf{C} &= [\mathbf{r}_1 \lambda_1 \cdots \mathbf{r}_n \lambda_n] \\ \mathbf{D} &= \left[\mathbf{z} + \sum_{k=1}^n \mathbf{r}_k \right]. \end{aligned} \quad (28)$$

Eigenvalues are $\lambda_k = p_k$. Static constant \mathbf{y}_0 gives output \mathbf{y}^* the proper value at the linearization point. In the following, we drop the $*$ symbol from the reduced model, for brevity.

The model order reduction procedure has the effect of grouping together or lumping modes that have similar eigenvalues. The lumped modes reasonably reproduce the diffusion system's smoothly varying frequency response. The authors also introduced a rule-based modal grouping method [11] to obtain (25); however, the analytical treatment required by that method makes it cumbersome when dealing with the full battery model (24). By comparison, frequency simulation is straightforward and a minimized cost function (26) is therefore preferred.

The reduction procedure requires that transfer functions have finite steady state, a condition satisfied by each of the infinite-dimensional diffusion terms of the voltage/current model, that is, terms two through five of (24). The first term of (24), related to SOC, has a single eigenvalue at the origin and is not reduced. Note that grouping the two electrodes' bulk solid concentration dynamics together in a single SOC term is necessary to make the linear model observable.

In [12], the voltage/current state variable model was constructed by separately fitting transfer functions for negative electrode solid diffusion, positive electrode solid diffusion, and electrolyte diffusion dynamics, giving model states $\mathbf{x} = [\text{SOC} \mathbf{x}_-^T \mathbf{x}_+^T \mathbf{x}_e^T]^T$. In cases in which eigenvalues for the negative and positive electrode states are closely matched, however, we find that positive and negative electrode diffusion dynamics may share the same set of eigenvalues, λ_{\pm} , with little loss in accuracy. Taking this approach, model states are $\mathbf{x} = [\text{SOC} \mathbf{x}_{\pm}^T \mathbf{x}_e^T]^T$ in this work.

D. Kalman Filter

The standard Kalman filter formulation assumes that the plant contains process noise w and measurement noise v in the form

$$\begin{aligned} \dot{\hat{\mathbf{x}}} &= \mathbf{A}\hat{\mathbf{x}} + \mathbf{B}u + \mathbf{G}w \\ y &= \mathbf{C}\hat{\mathbf{x}} + \mathbf{D}u + y_0 + v. \end{aligned} \quad (29)$$

State estimates $\hat{\mathbf{x}}$ are calculated from sensor measurements $u(t)$ and $y(t)$ as

$$\dot{\hat{\mathbf{x}}} = \mathbf{A}\hat{\mathbf{x}} + \mathbf{B}u + \mathbf{L}(y - y_0 - \mathbf{C}\hat{\mathbf{x}} + \mathbf{D}u). \quad (30)$$

The optimal filter gain \mathbf{L} is precalculated offline as a function of process noise covariance \mathbf{Q}_w , measurement noise covariance \mathbf{Q}_v , and process noise input matrix \mathbf{G} to minimize the steady-state error covariance

$$\mathbf{P} = \lim_{t \rightarrow \infty} E([\mathbf{x} - \hat{\mathbf{x}}][\mathbf{x} - \hat{\mathbf{x}}]^T). \quad (31)$$

E. Reference Current

State estimate $\hat{\mathbf{x}}(t)$ is used to predict a limiting current such that at future time $t + T$, internal battery parameter y (i.e., a concentration or potential) will reach limiting value y_{lim} (saturation/depletion, side reaction, etc.). For constant u , the linear

state equation may be integrated forward in time with explicit solution. The limiting current available for T seconds is

$$I_{\min/\max,T} = [\mathbf{CA}'\mathbf{B} + \mathbf{D}]^{-1} \{ (y_{\text{lim}} - y_0) - \mathbf{C}e^{\mathbf{A}T}\hat{\mathbf{x}} \}. \quad (32)$$

For the present system with $\lambda_1 = 0$

$$\mathbf{A}' = \text{diag} \left(T \quad \frac{1}{\lambda_2}(e^{\lambda_2 T} - 1) \quad \dots \quad \frac{1}{\lambda_n}(e^{\lambda_n T} - 1) \right). \quad (33)$$

Note that for this single-output system the square-bracketed term in (32) is scalar and no matrix inversion is required.

III. RESULTS AND DISCUSSION

Compared with empirical-based estimation algorithms [1], [2], the present electrochemical-based algorithm is complex and requires numerous model parameters. Electrochemical parameter identification [15], [16] is not discussed in this paper. The electrochemical algorithm is motivated by the fact that HEV battery packs, costing thousands of dollars per vehicle, are not used to their full power and energy capability because of the uncertainty about when damage or a sudden loss of power may occur in the real-time environment. The objective of the present modeling study is to demonstrate a practical method of controlling a battery to internal physiochemical constraints, thereby enabling an expanded range of power capability.

The battery simulated is a 6 Ah Li-ion cell, part of a 72-cell, 276 V nominal battery pack (45 kg, 37 L, 25 kW/18 s pulse discharge) built for the U.S. Department of Energy FreedomCAR program [17]. In previous work, the authors identified and validated a 313th-order nonlinear finite-volume model against constant current, transient pulse current, and driving cycle experimental data [18]. Model parameters for the 6 Ah cell are given in Table I. The authors subsequently formulated the low-order state-variable model (SVM) and validated it against the high-order FVM [12]. In this work, the nominal SVM uses five states to describe positive and negative electrode solid-state diffusion or concentration gradient dynamics and one state to describe electrolyte concentration gradient dynamics. An additional state describes SOC. This $5D_{s\pm}/1D_e$ SVM, with 0 to 10 Hz bandwidth, has eigenvalues

$$\lambda_{\text{SOC}} = 0, \quad \lambda_{\pm} = -[0.00704, 0.0606, 0.613, 6.10, 63.1], \\ \lambda_e = -0.0992 \text{ rad/s}.$$

The number of states is chosen to bring the reduced model residual error (24) within an acceptable error tolerance [12].

Sizing filter gain \mathbf{L} requires choices for \mathbf{Q}_w , \mathbf{Q}_v , and \mathbf{G} . This paper interprets w as current sensor noise and adjusts its relative influence on individual states with \mathbf{G} . With this interpretation, \mathbf{Q}_w is current sensor noise covariance and \mathbf{Q}_v is voltage sensor noise covariance, here, $\mathbf{Q}_w = (2 \text{ A})^2$ and $\mathbf{Q}_v = (0.025 \text{ V})^2$. In theory, the relative influence of process noise on individual states may be adjusted with individual elements of \mathbf{G} ; however, this paper finds that filter eigenvalues (eigenvalues of $\mathbf{A} - \mathbf{LC}$) deviate very little from model eigenvalues (eigenvalues of \mathbf{A}) irrespective of \mathbf{Q}_w , \mathbf{Q}_v , and \mathbf{G} with the exception of λ_{SOC} . The SOC eigenvalue, located at the origin in the open-loop model, takes on negative real values in the closed-loop filter. Attempts to move other filter eigenvalues to slightly faster locations (as

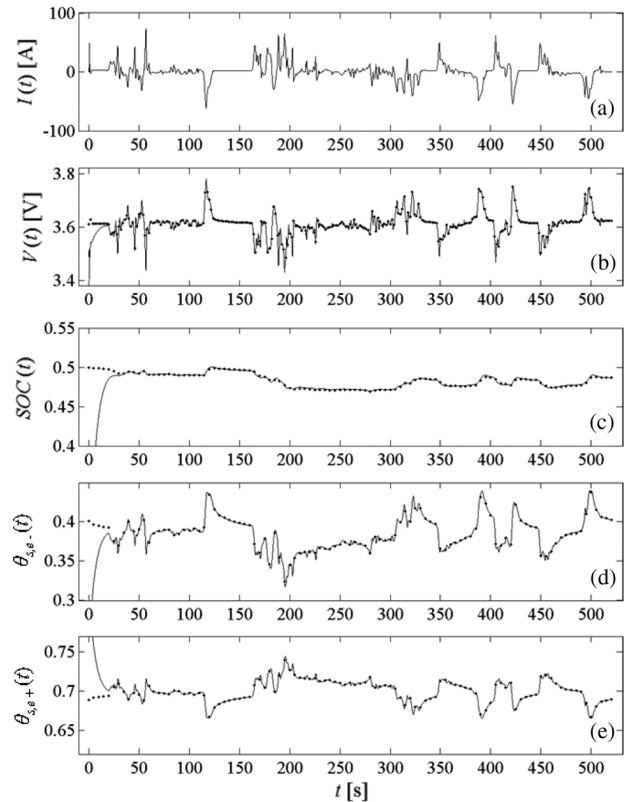


Fig. 2. UDDS driving cycle simulation: Nonlinear FVM model with 50% SOC initial condition (\bullet) and linear filter with 20% SOC initial condition ($-$). (a) Current profile. (b) Voltage response. (c) SOC. (d) Negative electrode average surface stoichiometry. (e) Positive electrode average surface stoichiometry.

little as $1.01 \times \lambda_{\pm}$) through pole placement causes state estimates to become overly sensitive to sensor noise.

Fig. 2 compares filter results with data generated by the nonlinear FVM simulating the Urban Dynamometer Driving Schedule (UDDS) for a hybrid electric mid-sized passenger car [18] at 50% SOC. The cycle consists mostly of short-duration, low-to-medium-rate current pulses for which the battery response is largely linear. In the simulation, filter states are initialized at $\hat{\mathbf{x}}(0) = [0.2 \ 0 \ \dots \ 0]^T$, i.e., 20% SOC with zero solid and electrolyte phase concentration gradients. The filter gain is sized with $\mathbf{G} = [0.005 \ \dots \ 0.005]$, giving 20 to 30 s (20–30 s) convergence to proper SOC [see Fig. 2(c)]. To simplify presentation, Fig. 2(d) and (e) give solid phase surface concentration distributions, $c_{s,e}(x,t)$, as electrode-averaged surface stoichiometries

$$\theta_{s,e}(t) = \frac{1}{\delta c_{s,\max}} \int_0^{\delta} c_{s,e}(x,t) dx. \quad (34)$$

Surface stoichiometries rise and fall much faster than SOC as they are more closely coupled to recent charge/discharge history. Overshoot in SOC and surface stoichiometry can occur when filter states $\hat{\mathbf{x}}_{\pm}$, and/or $\hat{\mathbf{x}}_e$ are initialized to nonzero values, but convergence is still obtained in 20–30 s.

Faster converging filters yield noisy estimates when 2 A and 25 mV current and voltage sensor noise, respectively, are included in the simulation. These noise levels are chosen to rep-

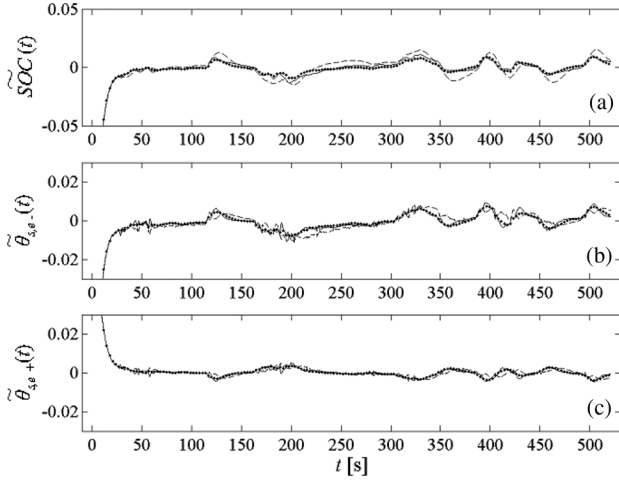


Fig. 3. Filter error for UDDS driving cycle simulation using filters of various order: $5D_{s\pm}/0D_e$ (6 state) filter (\bullet), $4D_{s\pm}/0D_e$ (5 state) filter ($-$), $3D_{s\pm}/0D_e$ (4 state) filter ($- \cdot -$). SOC initial conditions: 50% and 20%, respectively, for nonlinear FVM model and linear filters.

resent low-cost sensors for an actual hybrid vehicle. With lower noise sensors, the filter gains could be increased to reduce convergence time without impacting estimate accuracy. The convergence rate of 20–30 s, however, is reasonable for the application. Typically, the initial SOC error is much smaller than the 30% used in Fig. 2.

In many situations, and particularly for input currents with a negligible dc component such as the UDDS cycle current profile shown in Fig. 2(a), lower order filters also provide good performance. Electrolyte diffusion dynamics, impacting the voltage response of the present battery only for sustained medium-to-high-rate currents, may be dropped from the filter, and electrode transcendental transfer functions may be fit with 3rd and 4th order rational transfer functions rather than fifth-order functions. Fig. 3 compares SOC and surface stoichiometry errors for filters constructed from $5D_{s\pm}/0D_e$, $4D_{s\pm}/0D_e$, and $3D_{s\pm}/0D_e$ models. The $4D_{\pm}/0D_e$ model has eigenvalues

$$\lambda_{\text{SOC}} = 0, \lambda_{\pm} = -[0.00828, 0.0127, 2.31, 41.5] \text{ rad/s}$$

and the $3D_{s\pm}/0D_e$ model has eigenvalues

$$\lambda_{\text{SOC}} = 0, \lambda_{\pm} = -[0.0116, 0.581, 27.3] \text{ rad/s.}$$

A slight difference is evident between the three filters' performance on the UDDS cycle.

In Fig. 4, the battery is discharged from 100% SOC via 60 A pulses of 10 s duration with a 10 s rest between each pulse. The discharge may be interpreted as a 30 A constant current discharge superposed with ± 30 A perturbations. The DC component of the current profile causes an electrolyte concentration gradient to be established after approximately 20 s. Comparison of the $5D_{s\pm}/1D_e$ and the $5D_{s\pm}/0D_e$ filters shows that an additional 1%–2% in SOC error and 1% in $\theta_{s,e}$ error is introduced by dropping electrolyte phase dynamics from the filter. Reducing the electrode model from 5 to 3 states introduces an additional 1% error in $\theta_{s,e-}$ but affects $\theta_{s,e+}$ and SOC estimates very little.

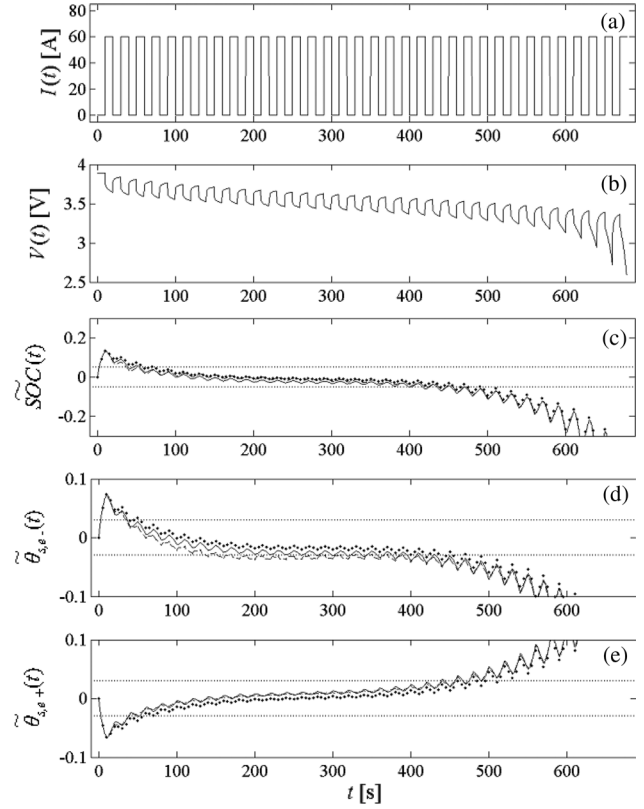


Fig. 4. 10-s, 60 A pulse discharge profile initiated from 100% SOC: (a) current profile; (b) voltage response of nonlinear FVM model; (c–e) filter errors: $5D_{s\pm}/1D_e$ (7 state) filter (\bullet), $5D_{s\pm}/0D_e$ (6 state) filter ($-$), $3D_{s\pm}/0D_e$ (4 state) filter ($- \cdot -$). Horizontal dotted lines denote $\pm 5\%$ SOC error threshold in (c) and $\pm 3\%$ surface stoichiometry error thresholds in (d) and (e).

The discharge presented in Fig. 4 exhibits significant nonlinearities at the beginning ($t < 75$ s) and end of the discharge ($t > 450$ s) where the linear filter performs poorly. Equilibrium potentials U_+ and U_- , functions of surface stoichiometry (not bulk SOC), represent the dominant nonlinearity of the battery and the linear filter performs well so long as $\theta_{s,e-}$ and $\theta_{s,e+}$ remain within approximately ± 0.15 of their 50% SOC linearization points. Note that surface stoichiometry, and thus equilibrium potential, will be a function of SOC only at rest, in the absence of solid-state concentration gradients. At rest, the linear filter is accurate in the interval $27\% < \text{SOC} < 72\%$. Under discharge or charge, however, surface dynamics can significantly lead bulk dynamics (i.e., SOC) and for the particular pulse discharge case shown in Fig. 4, the filter performs well from 92% SOC ($t = 75$ s) to 49% SOC ($t = 450$ s).

This paper explores two different filter applications of practical value for HEV control: 1) calculation of an instantaneous “do not exceed” current that, in coordination with motor inverter power electronics, is intended to prevent battery damage and 2) prediction of maximum current available for T seconds that, in coordination with vehicle supervisory controllers, enables efficient and reliable HEV powertrain control. Depending upon computational power, embedded controllers may implement these algorithms either on a single-cell or a complete-battery-pack basis, and the latter is expected to require a more conservative approach when setting constraint limits because of

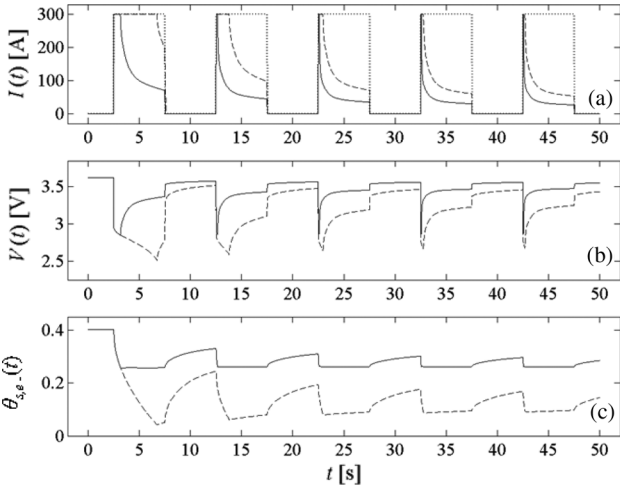


Fig. 5. 5-s, 300 A nominal pulse discharge profile (...) limited by $\theta_{s,e-} \geq 0.25$ maximum reference current (—) and $\theta_{s,e-} \geq 0.03$ maximum reference current (---). 50% SOC initial condition.

cell-to-cell variation. (Given safety issues associated with overcharging, note that it is already standard practice to measure the voltage of every cell in a Li-ion battery pack.)

In the following, state estimates are provided by the $5D_{s\pm}/1D_e$ (7 state) linear filter. Limiting currents are calculated using (32), where $T = 0$ for the instantaneous current limit and $T = 10$ s for prediction of future available current. Simulations of the 6 Ah battery show that negative electrode surface depletion limits the discharge performance before the occurrence of either positive electrode saturation or electrolyte depletion [18]. Meant to signal end of discharge, the manufacturer's 2.7 V minimum voltage limit can occur with $\theta_{s,e-}$ anywhere in the range [0.03, 0.3], depending on discharge current rate, SOC, and recent charge/discharge history. In other words, sometimes the battery can reach the 2.7 V "limit" even though the electrode surface is not yet fully depleted. To improve discharge power, a reference current may be used to control the battery to an electrode surface stoichiometry limit of $\theta_{s,e-} \geq 0.03$ during discharge.

Fig. 5 presents simulation results in which a nominal current profile, I_{nom} , consisting of 300 A discharge pulses of 5 s each, is limited using the control law $I(t) = \min(I_{\text{nom}}(t), I_{\text{max}}^{\theta_{s,e-}}(t))$. Simulations are presented for two different negative electrode surface stoichiometry limits, 0.03 and 0.25. The linear filter provides an imprecise, albeit conservative, reference current at the 0.03 limit as a result of plant nonlinearity at this low stoichiometry. Filter mismatch due to model linearization is, using equilibrium as a first approximation, predominantly caused by error in open-circuit voltage

$$\tilde{V}_{\text{OC}}(\text{SOC}) = V_{\text{OC}} \Big|_{50\%} + [\text{SOC} - 0.5] \times \frac{\partial V_{\text{OC}}}{\partial \text{SOC}} \Big|_{50\%} - V_{\text{OC}}(\text{SOC}). \quad (35)$$

The negative electrode's contribution to (35) is

$$-\tilde{U}_-(\theta) = -U_- \Big|_{50\%} - [\theta - \theta_{50\%}] \times \frac{\partial U_-}{\partial \theta} \Big|_{50\%} + U_-(\theta) \quad (36)$$

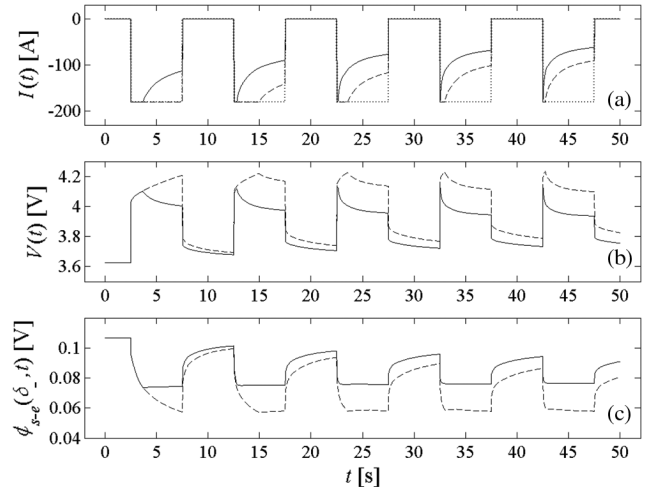


Fig. 6. 5-s, 180 A nominal pulse charge profile (...) limited by negative electrode $\phi_{s-e} \geq 0.082$ V minimum reference current (—) and $\phi_{s-e} \geq 0.07$ V minimum reference current (---). 50% SOC initial condition.

or 0.272 V error at $\theta = 0.03$, a large amount. If current is limited within a stoichiometry range $\theta_{50\%} \pm 0.15$ where the $U_-(\theta)$ linearization contributes less than 8 mV error, the reference current is more precise. Fig. 5(c) shows that discharge may be tightly controlled to a $\theta_{s,e-} \geq 0.25$ limit, nearer to the filter's linearization point.

Charge performance of the present cell is limited by the manufacturer's 3.9 V maximum voltage limit, though other Li-ion cells are sometimes charged as high as 4.2 V. The 3.9 V limit is far from electrode saturation/depletion, and is more likely intended to prolong battery life by slowing or avoiding side reactions that occur during charging at high voltages. One such side reaction is lithium plating at the negative electrode surface, predicted to occur in the negative electrode when $\phi_{s-e} = \phi_s - \phi_e < U_{Li,s}$, with equilibrium potential $U_{Li,s} = 0$ [5], [19]. Rather than insert into electrode active material particles, Li^+ ions from the electrolyte solution can form a solid Li film on the particle surface. If the manufacturer's 3.9 V maximum limit is to be respected, the FVM predicts a worst-case phase potential difference $\phi_{s-e} = 82$ mV occurring at the negative electrode/separator interface ($x = \delta_-$) during slow charging near 100% SOC.

In Fig. 6, the nominal 5-s 180 A pulse charging profile is limited by the afore-mentioned phase potential difference, that is, the battery is charged at the rate $I(t) = \max(I_{\text{nom}}(t), I_{\text{min}}^{\phi_{s-e}^{x=\delta_-}}(t))$. With control limits $\phi_{s-e}^{x=\delta_-} \geq 82$ mV and $\phi_{s-e}^{x=\delta_-} \geq 70$ mV, the system charges, respectively, 8 mV and 13 mV beyond the specified limit as a result of plant nonlinearities, but it still stays well above the theoretical limit, $U_{Li,s} = 0$. Without simulation, this phase potential difference error may again be estimated under the assumption of equilibrium where overpotential is neglected, leaving $\phi_{s-e,-} \approx U_-$. Equation (36) predicts 9 and 15 mV error for the 82 and 70 mV control limits, respectively, slightly greater than the overshoot error shown in Fig. 6. While some care must be exercised in setting control limits, the opportunity clearly exists to pulse charge the battery beyond 3.9 V and still be conservative with respect to the lithium plating side reaction.

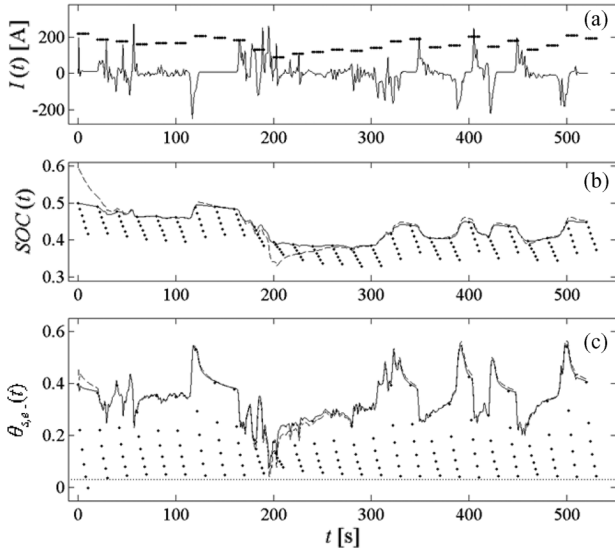


Fig. 7. 4xUDDS driving cycle with 10-s maximum current discharge events simulated once per 20 s: Model with 50% SOC initial condition (—), Filter with 60% SOC initial condition (---), $I_{\max,10\text{ s}}$ discharge events (\bullet). $I_{\max,10\text{ s}}$ calculated with $\theta_{s,e-} = 0.03$ end of discharge condition, shown in (c) with horizontal dotted line.

TABLE II

STANDARD DEVIATION (RELATIVE TO $\theta_{s,e-} = 0.03$ LIMIT) AND MINIMUM VALUE OF $\theta_{s,e-}$ AT END OF $I_{\max,10\text{ s}}$ DISCHARGE EVENTS DURING 4xUDDS SIMULATIONS SIMILAR TO THAT PRESENTED IN FIG. 7. $I_{\max,10\text{ s}}$ PREDICTED BY FILTERS OF VARYING ORDERS

Model	# States	$\sigma(\theta_{s,e}(T) - 0.03)$	$\min(\theta_{s,e}(T))$
$3D_{s\pm}/0D_e$	4	0.01953	0.000568
$3D_{s\pm}/1D_e$	5	0.0245	< 0
$4D_{s\pm}/0D_e$	5	0.00908	0.0379
$4D_{s\pm}/1D_e$	6	0.01254	0.0377
$5D_{s\pm}/0D_e$	6	0.00818	0.0392
$5D_{s\pm}/1D_e$	7	0.01276	0.0316

In addition to instantaneous limits, the reference current governor can predict maximum discharge current sustainable for some fixed time into the future, intended as a feed-forward input to powertrain supervisory control. The method is also applicable in the charge direction. Using $\theta_{s,e-} = 0.03$ as end of discharge limit and $T = 10\text{ s}$ in (32), Fig. 7 shows $I_{\max,10\text{ s}}$ discharge events simulated once every 20 s during a more severe UDDS cycle with four times the input current of the nominal UDDS cycle [see Fig. 2(a)]. The filter, initialized with +10% SOC error, converges in 20–30 s. The first $I_{\max,10\text{ s}}$ discharge event overshoots the $\theta_{s,e-} = 0.03$ end of discharge condition as a result of the initial error; however, after 20 s, the maximum discharge current is accurately predicted. Following several strong discharge pulses from 160–200 s, some SOC estimation error is evident, caused by low $\theta_{s,e-}$ and accompanying nonlinear voltage response. Filter estimates recover as concentration gradients relax. Maximum current, underpredicted during this excursion, also recovers to good accuracy for the remainder of the cycle.

Table II quantifies the ability of lower order filters to forecast $I_{\max,10\text{ s}}$ with end of discharge condition $\theta_{s,e-} = 0.03$ on the 4xUDDS cycle following the initial convergence transient. Only slight performance is lost by dropping the electrolyte diffusion state from the filter and/or by reducing the number of

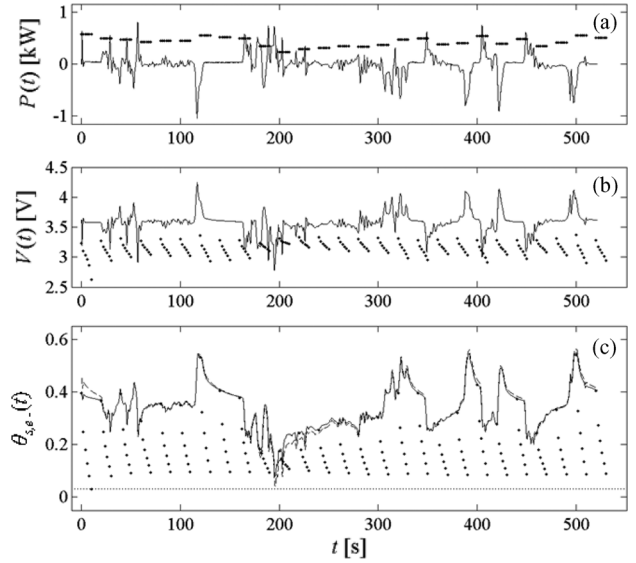


Fig. 8. 4xUDDS driving cycle with 10-s maximum power discharge events simulated once per 20 s: Model with 50% SOC initial condition (—), Filter with 60% SOC initial condition (---), $P_{\max,10\text{ s}}$ discharge events (\bullet). $P_{\max,10\text{ s}}$ calculated with 2.65 V and $\theta_{s,e-} = 0.03$ end of discharge conditions, the latter shown in (c) with horizontal dotted line.

electrode states from 5 to 4, but further reduction to 3 electrode states greatly increases the variability in $\theta_{s,e-}$ reached at the end of each discharge event simulation. The $3D_{s\pm}/0D_e$ filter sometimes predicts discharge rates that are not sustainable, where surface stoichiometry is depleted in less than 10 s. The fourth-order $3D_{s\pm}/0D_e$ filter is still a feasible candidate, though only if used with a more conservative end of discharge stoichiometry limit, perhaps $\theta_{s,e-} = 0.06$.

Available current prediction is attractive because of the explicit manner in which the linear problem may be solved online; however, an available power prediction would be more meaningful in the vehicle environment. A precise power estimate would require an iterative nonlinear solver (such as the bisection search) performing constant power forward time simulation as discussed in [20]. Alternatively, a conservative discharge power estimate may be explicitly calculated as

$$P_{\max,T} = (I_{\max,T})(V_{\min}) \quad (37)$$

where V_{\min} represents the lowest voltage occurring during the maximum current event, i.e., at the end. A conservative charge power estimate may be explicitly calculated as

$$P_{\min,T} = (I_{\min,T})(U_+ - U_- + DI_{\min,T}) \quad (38)$$

where U_+ and U_- are equilibrium potentials (functions of electrode surface stoichiometry at the current collectors (15), not functions of SOC) and D is the static gain component of the voltage/current state variable model. The voltage ($U_+ - U_- + DI_{\min,T}$) will be the lowest voltage over the course of an $I_{\min,T}$ event, occurring at the very beginning. Fig. 8 presents the 4xUDDS simulation with $P_{\max,10\text{ s}}$ events simulated every 20 s. With the exception of the first event influenced by filter initial conditions, power capability predicted from (37) is, on average, 12% lower than actual available power. Less conservative

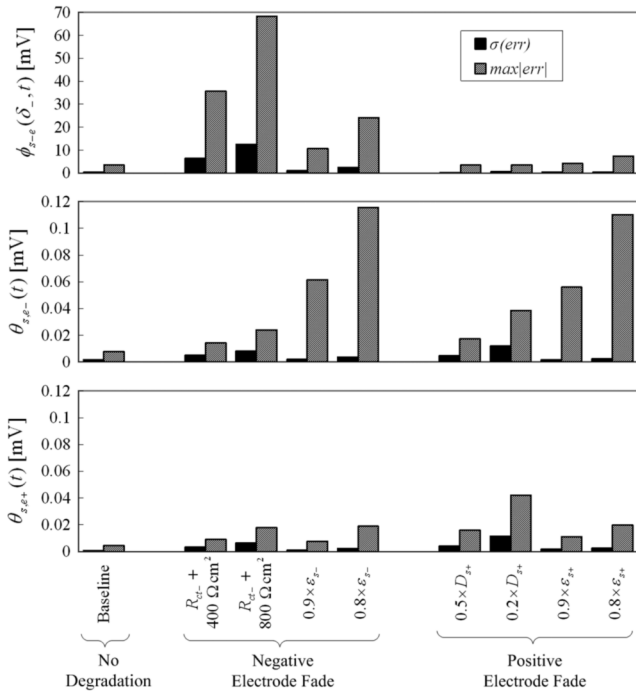


Fig. 9. Standard deviation (solid bars) and maximum (gray bars) of estimation error for a UDDS driving cycle. Plant parameters are modified to simulate a degraded battery at middle and end of life.

power prediction may be obtained using a nonlinear reference governor at the expense of added computational overhead.

The algorithm presented here is not adaptive, meaning that some provision must be taken to ensure safe operation throughout the life of the battery. Many degradation mechanisms are described in the literature for Li-ion batteries, causing loss of discharge/charge capacity, impedance growth, or both. Examples include loss of active material sites in both electrodes [21], growth of a solid/electrolyte interface layer on the negative electrode [22], and material structural changes causing increased diffusion impedance at the positive electrode [23]. To explore performance of the filter with a degraded battery, Fig. 9 gives the standard deviation and maximum error of the nominal filter in predicting various control parameters for the UDDS cycle [see Fig. 2(a)]. Twenty percent energy or power loss is a typical end of life threshold for vehicle traction batteries [17]. Battery degradation is simulated by modifying the plant parameters to the extent that they cause 10% and 20% energy loss (reduction of usable active material volume fraction ε_{s-} and ε_{s+}) and/or power loss (film impedance growth $R_{ct} + R_{film}$ at the negative and diffusion impedance growth $1/D_s$ at the positive). Fig. 9 shows tolerable filter error for 10% degradation; however, filter error is large at 20% degradation, particularly when: 1) negative electrode phase potential difference is to be controlled in the presence of a large film resistance on that electrode or 2) negative electrode surface stoichiometry is to be controlled in the presence of large negative or positive electrode capacity fade. Positive electrode surface stoichiometry remains well predicted under the various fade scenarios explored. The positive electrode is “more” observable than the negative electrode, indicated by the balanced observability/controllability

Grammian in [12], because of its more than sevenfold stronger equilibrium potential dependency on surface stoichiometry.

An adaptive algorithm is desirable if computational complexity can be kept reasonably low. Alternatively, a simpler approach to improve robustness might be to identify the linear filter at the middle of battery life, when $\sim 10\%$ fade has already occurred. In this way, mismatch would be less severe at end of life.

IV. CONCLUSION

This paper shows how filters with low order (4 to 7 states) may be designed from a fundamental Li-ion battery model to control battery charge/discharge up to physical saturation/depletion and side reaction limits rather than more conservative fixed-voltage limits at the battery terminals. The linear filter, based on a 50% SOC linearized model, performs well so long as electrode surface stoichiometries stay within rest values corresponding to 30%–70% SOC. During discharge or charge, however, electrode surface dynamics can significantly lead bulk (SOC) dynamics and a severe discharge/charge event may cause nonlinear voltage response even with SOC near the 50% linearization point. Following such an event, the linear filter recovers as electrode solid-state concentration gradients relax.

Unlike previous electrochemical models formulated using spatial discretization techniques, the present reduced order model enjoys computational efficiency comparable to equivalent circuit models. Expressed as a maximum current available for a finite time horizon, the reference governor predicts margin with respect to saturation/depletion and side reaction conditions in a manner practical for integration with HEV powertrain supervisory control. Instantaneous operating limits generally occur in nonlinear regions of battery operation, for which a nonlinear filter would be better suited than the linear filter. Despite the error associated with the linear filter, the present method enables pulse charging beyond the manufacturer’s maximum voltage limit while maintaining a conservatism with respect to the lithium plating side reaction. In the future, adaptivity or online parameter estimation is desired to better accommodate negative electrode model mismatch when the battery is severely faded near end of life.

REFERENCES

- [1] M. W. Verbrugge and B. J. Koch, “Generalized recursive algorithm for adaptive multiparameter regression,” *J. Electrochem. Soc.*, vol. 153, pp. A187–A201, 2006.
- [2] G. L. Plett, “Extended Kalman filtering for battery management systems of LiPB-based HEV battery packs—Part 3. State and parameter estimation,” *J. Power Sources*, vol. 134, pp. 277–292, 2004.
- [3] G. M. Ehrlich, “Lithium ion batteries,” in *Handbook of Batteries*, 3rd ed. New York: McGraw-Hill, 2002, pp. 35.53–35.59.
- [4] Lithium Technology Corporation, Plymouth Meeting, PA, “Ultra High Power Cells: 7.5 Ah UHP-341450,” 2006. [Online]. Available: <http://www.lithiumtech.com/StandardCells.html>
- [5] M. Doyle, T. Fuller, and J. Newman, “Modeling of galvanostatic charge and discharge of the lithium/polymer/insertion cell,” *J. Electrochem. Soc.*, vol. 140, pp. 1526–1533, 1993.
- [6] T. Fuller, M. Doyle, and J. Newman, “Simulation and optimization of the dual lithium ion insertion cell,” *J. Electrochem. Soc.*, vol. 141, pp. 1–10, 1994.
- [7] A. Bemporad, “Reference governor for constrained nonlinear systems,” *IEEE Trans. Autom. Control*, vol. 43, pp. 415–419, 1998.

- [8] J. Sun and I. V. Kolmanovskiy, "Load governor for fuel cell oxygen starvation protection: A robust nonlinear reference governor approach," *IEEE Trans. Control Syst. Technol.*, vol. 13, no. 6, pp. 911–920, Nov. 2005.
- [9] A. Tenno, R. Tenno, and T. Suntio, "Charge-discharge behaviour of VRLA batteries: Model calibration and application for state estimation and failure detection," *J. Power Sources*, vol. 103, pp. 42–53, 2001.
- [10] O. Barbarisi, F. Vasca, and L. Glielmo, "State of charge Kalman filter estimator for automotive batteries," *Control Eng. Practice*, vol. 14, pp. 267–275, 2006.
- [11] K. A. Smith, C. D. Rahn, and C.-Y. Wang, "Model order reduction of 1D diffusion systems via residue grouping," *ASME J. Dyn. Syst., Meas., Control*, vol. 130, pp. 11–12, 2008.
- [12] K. A. Smith, C. D. Rahn, and C.-Y. Wang, "Control-oriented 1D electrochemical model of lithium ion battery," *Energy Conv. Manage.*, vol. 48, pp. 2565–2578, 2007.
- [13] T. Jacobsen and K. West, "Diffusion impedance in planar, cylindrical and spherical symmetry," *Electrochem. Acta*, vol. 40, pp. 255–262, 1995.
- [14] I. Ong and J. Newman, "Double-layer capacitance in a dual lithium ion insertion cell," *J. Electrochem. Soc.*, vol. 146, pp. 4360–4365, 1999.
- [15] G. Sikha and R. E. White, "Analytical expression for the impedance response of an insertion electrode cell," *J. Electrochem. Soc.*, vol. 154, pp. A43–A54, 2007.
- [16] S. Santhanagopalan, Q. Guo, and R. E. White, "Parameter estimation and model discrimination for a lithium-ion cell," *J. Electrochem. Soc.*, vol. 154, pp. A198–A206, 2007.
- [17] "FreedomCAR Battery Test Manual for Power-Assist Hybrid Electric Vehicles," Oct. 2003, DOE/ID-11069.
- [18] K. A. Smith and C.-Y. Wang, "Solid state diffusion limitations on pulse operation of a lithium ion cell for hybrid electric vehicles," *J. Power Sources*, vol. 161, pp. 628–639, 2006.
- [19] M. W. Verbrugge and B. J. Koch, "Effect of large negative potentials and overcharge on the electrochemical performance of lithiated carbon," *J. Electroanalytical Chem.*, vol. 436, pp. 1–7, 1997.
- [20] G. L. Plett, "High-performance battery-pack power estimation using a dynamic cell model," *IEEE Trans. Veh. Technol.*, vol. 53, no. 5, pp. 1586–1593, Sep. 2004.
- [21] S. Santhanagopalan, Q. Zhang, K. Kumaresan, and R. E. White, "Parameter estimation and life modeling of lithium-ion cells," *J. Electrochem. Soc.*, vol. 155, pp. A345–A353, 2008.
- [22] P. Ramadass, B. Haran, P. M. Gomadam, R. E. White, and B. N. Popov, "Development of first principles capacity fade model for li ion cells," *J. Electrochem. Soc.*, vol. 151, pp. A196–A203, 2004.
- [23] D. Dees, E. Gunen, D. Abraham, A. Jansen, and J. Prakash, *J. Electrochem. Soc.*, vol. 152, pp. A1409–A1417, 2005.



Kandler A. Smith (M'07) received the Ph.D. degree in mechanical engineering from the Pennsylvania State University, University Park, in 2006.

He is a Senior Engineer in Transportation Technologies and Systems at the U.S. Department of Energy's National Renewable Energy Laboratory, Golden, CO. Prior to graduate school, he spent four years with United Technologies Corporation—Pratt & Whitney developing jet engine control systems for a vertical take-off and landing aircraft.

Dr. Smith is an active member of the Electrochemical Society and the Society for Automotive Engineers.



Christopher D. Rahn received the Ph.D. degree from the University of California, Berkeley, in 1992.

He is currently a Professor of Mechanical Engineering at the Pennsylvania State University, University Park.

Dr. Rahn was a recipient of a prestigious Office of Naval Research Young Investigator Award for his research work on the modeling, analysis, and control of mechatronic systems garnered, which has resulted in 1 book, over 100 refereed publications, and several patents. He was an Associate Editor of the *ASME Journal of Dynamic Systems, Measurement, and Control* and is currently an Associate Editor of the *ASME Journal of Vibration and Acoustics*, the Chair of the ASME Technical Committee on Vibration and Sound, and a Fellow of ASME.

Dr. Rahn was a recipient of a prestigious Office of Naval Research Young Investigator Award for his research work on the modeling, analysis, and control of mechatronic systems garnered, which has resulted in 1 book, over 100 refereed publications, and several patents. He was an Associate Editor of the *ASME Journal of Dynamic Systems, Measurement, and Control* and is currently an Associate Editor of the *ASME Journal of Vibration and Acoustics*, the Chair of the ASME Technical Committee on Vibration and Sound, and a Fellow of ASME.



Chao-Yang Wang is a Distinguished Professor of Mechanical Engineering and Professor of Materials Science and Engineering at the Pennsylvania State University, University Park. He has been the founding director of the Electrochemical Engine Center (ECEC) since 1997. He holds 16 U.S. and international patents and has published nine book chapters and reviews as well as over 150 journal articles. His research interests cover the transport and materials aspects of batteries and fuel cells.

Dr. Wang is a fellow of ASME.